communications materials

Article

https://doi.org/10.1038/s43246-024-00570-9

Microchannel pressure sensor for continuous and real-time wearable gait monitoring

Jung-Bin Ahn [1,2,5], Byungseok Yoo[3,5], Darryll J. Pines[3], Chia-Ying Kuo[1], Mingyi Wang[1], Naga Sai Gouthami Bejjanki[1] & Soaram Kim [1,2,4] ✉

A highly sensitive and multi-functional pressure sensor capable of continuous pressure readings is greatly needed, particularly for precise gait pattern analysis. Here, we fabricate a sensitive and reliable pressure sensor by employing eutectic gallium indium (EGaIn) liquid metal as the sensing material and EcoFlex 00-30 silicone as the substrate, via a low-cost process. The device architecture features a microchannel, creating two independent sensing devices, and the mechanical properties of the substrate and sensing material contribute to high stretchability and flexibility, resulting in a sensitivity of 66.07 MPa^{-1} and a low measurement resolution of 0.056 kPa. The sensor detects applied pressure accurately and can distinguish pressure distribution across a wide area. We demonstrate high efficiency for monitoring human walking gait at various speeds when a single sensor is attached to the foot, and can differentiate between walking postures. This device has strong potential for clinical and rehabilitation applications in gait analysis.

In recent times, the advancement of pressure sensor technology has been driven by the rapid growth of industries such as automotive, aerospace, healthcare, and robotics, which require accurate pressure sensing measurements[1–3]. Furthermore, there is a growing need to detect a wide range of small to large pressures in bodies by applying wearable and implantable devices[4–6]. In this regard, various materials and methods have been explored to improve pressure sensing performances, including high accuracy, sensitivity, and durability. For example, high-conductivity materials such as carbon nanotube (CNT) and graphene were adapted as sensing materials for promising piezoelectric or piezoresistive pressure sensors[7–13]. The reported sensors exhibited exceedingly low detection limits, which can be attributed to the subtle resistance changes of the sensing materials under minor pressure variations. Still, the quantification range was limited to tens of kPa because of the dimensional breakage of the sensors under high pressure. Capacitive-type pressure sensors using polydimethylsiloxane (PDMS) or ionic liquid as sensing materials showed a wide detection range from small to high pressure, as they could easily vary their dimensions under pressure, thereby changing the output capacity[14–17]. However, to improve the sensing performance, the microstructure of the sensors should be controlled sophisticatedly using highly pricey processes such as the etching and lithography process, resulting in cost-effective issues. Thus, an innovative fabrication process with low-cost and extra-deformable materials is required to fabricate practically applicable pressure sensors.

Recently, liquid-state electronics using liquid metal have emerged as a promising approach for pressure sensors to overcome the limitations of the existing sensors. Eutectic gallium indium (EGaIn) is one of the common liquid metals used in electronic devices as it maintains low viscosity at near room temperature (1.99×10^{-3} Pa s) and has excellent electrical conductivity and high readability, allowing it to detect pressure from small to large range[18–20]. To fully utilize these characteristics of EGaIn as a sensing material, choosing a suitable substrate with durability and susceptible deformability under extreme stimuli is crucial to ensure the effective transmission of small external stimuli (the pressure) to the sensing materials. In this context, the deformable elastomers have opted as sensor substrates to substitute the stiff substrate like a silicon wafer. The commercialized elastomers, including Sylgard[21], Dragonskin[22], or EcoFlex[23], were commonly used owing to their mechanical stability, chemical inertness, and biocompatibility. Among them, EcoFlex is a preferred choice due to its high flexibility, printability, and resistance to water and tearing[23,24]. Many researchers have reported achieving soft and delicate pressure sensors incorporating EGaIn into EcoFlex, expecting them to perform synergistically as pressure sensors due to the advantages of their own materials'

[1]Department of Electrical and Computer Engineering, Texas A&M University, College Station, TX, 77843, USA. [2]Center for Remote Health Technologies and Systems, Texas A&M University, College Station, TX, 77843, USA. [3]Department of Aerospace Engineering, University of Maryland, College Park, MD, 20742, USA. [4]Department of Biomedical Engineering, Texas A&M University, College Station, TX, 77843, USA. [5]These authors contributed equally: Jung-Bin Ahn, Byungseok Yoo. ✉e-mail: soaramk@tamu.edu

properties[25–27]. In general, a curvy-shaped microchannel with a narrow diameter filled with EGaIn is used to fabricate the pressure sensors in order to enhance the sensing performance[28,29]. However, this process includes complex and expensive techniques such as laser cutting, surface-controlled coating, or various etching processes with lithography that should be avoided to promote scale-up industrialization. Despite some papers reporting the fabrication of soft matrix/EGaIn-based torsion, strain, and touch sensors via a simple liquid metal injection method and achieving high sensitivity[29,30], their applicability is limited due to restrictive microchannel design that can sense a single pressure at a time. While multi-pressure sensing ability within a single device has been reported by adapting a grid/parallel structure of microchannel design[31,32], however, this approach is impractical for real-world applications, especially for a wearable device, necessitating complex data handling methods, incurring higher costs, and requiring the use of several wire connections and multiplexers when attaching numerous devices to the sensing area. Hence, there is a strong need for a multi-pressure detection method with a single device while avoiding any discomforts of employing multiple wire connections.

As one of the streams, we previously developed an EGaIn-EcoFlex-based multi-strain sensor, avoiding complex fabrication steps[33,34]. The microchannels in the sensor were easily prepared by a 3D-printed mold with unique architecture. The microchannels in a single device detected various applied strains simultaneously, showing the possibility of an innovative next-generation multi-strain sensor. Building upon this achievement, we adopted the approach of developing two different sensing channels divided into five sections within a single device. The design enables comprehensive analysis of pressure, covering both static and dynamic conditions, facilitating the analysis of pressure applied location and continuous monitoring of the center of pressure movement. The sensors were tested as a practical application for a gait monitoring sensor, exhibiting excellent performance: the sensor analyzed a pressure distribution on foot while walking and distinguished certain patterns between correct walking posture and incorrect walking posture, irrespective of the walking speed. Hence, the designed pressure sensors hold significant potential as a platform for large-dimensional sensors capable of multi-functional pressure detection in disabilities and rehabilitation engineering areas by leveraging the cost-effective fabrication method employing readily available materials.

Results and discussion

Architecture of microchannel design

The proposed pressure sensor, featuring optimized microchannels filled with EGaIn on an EcoFlex substrate, showcases a unique approach to microchannel architecture. The microchannels of the proposed sensor were fabricated based on our reported procedure[33,34], with the experimental details briefly depicted in Fig. 1. EcoFlex 00-30 prepolymer was poured into the plastic mold and left to cure at room temperature for 4 h to obtain the open microchannel. The substrate with an open microchannel was attached to the spin-coated silicone backing layer in an upside-down direction to cover the microchannels. The air-filled microchannels were obtained by following the curing of the backing layer. Liquid EGaIn alloy was introduced to the microchannels using a syringe injection method, and the fabrication was completed by connecting copper wires to each sensing channel. All the detailed steps for the fabrication were also described in the Method part. The microchannel dimensions were analyzed, as depicted in Supplementary Fig. 1a. The average width and height measured 254 and 130 μm, respectively, with less than a 2.5% error compared to the intended dimensions of 250 × 125 μm. The encapsulation of EGaIn in the microchannel was confirmed by extremely stretching the sensor, as shown in Supplementary Fig. 1b.

Figures 2a and b illustrate the pressure sensor design, and Fig. 2c shows pictures of the pressure measurement setup and the sensor. The sensor consisted of two sensing channels, individually marked in red and green lines in Fig. 2a. The sensor configuration can be systematically divided into five discrete sections, as depicted in Fig. 2a, based on the approach to architecting microchannel. Each section consists of 12 microchannels in total, with the combination of sensing channel 1 (green line) and sensing channel 2 (red line). The number of microchannels of sensing channel 1 (green lines) increases from two to ten with an interval of two, while that of sensing channel 2 (red lines) decreases from ten to two. This proposed design allows the sensor to distinguish five different sections very well, resulting in the detection of pressure location. Figure 2b shows the detailed dimensional information on the sensor design, including the spacing between the microchannels (500 μm) and the sections (1.5 mm). To test the sensor performance, various pressures were applied to the sensor by a custom-built pressing tester, ranging from 0 to 0.1 MPa, as shown in Fig. 2c.

Sensor performance analysis

Figure 3 shows the performance testing results of the pressure sensor. The output resistance R_1 and R_2 represent the response changes of sensing channel 1 and sensing channel 2, respectively, under a gradual loading/unloading pressure test, as shown in Fig. 3a. The detailed information on loading/unloading pressures to each section in the sensor is explained in Supplementary Fig. 2a. Although the same pressure of up to 0.1 MPa is subjected to each section in the sensor, the responses of sensing channel 1 (R_1, indicated by the black line) and sensing channel 2 (R_2, represented by the red line) were different across the sections. Notably, in the context of the pressure loading/unloading test, it is evident that the output resistance changes of R_1 exhibited a gradual rise from section 1 to 5, while R_2 registered a decline. This is because of our approach to architecting microchannel in pressure sensors, as depicted in Fig. 2a. When pressure is applied to a specific section, it gets uniformly distributed across every microchannel with that section in the sensor, irrespective of their sensing channel affiliations. This uniform distribution induces a consistent resistance change across these microchannels. Thus, the total resistance changes in sensing channels 1 and 2 within the pressed section are the combined changes from each microchannel. Based on this, the pressure location index ($\Delta R/(\Delta R_1 + \Delta R_2)$) can be calculated by considering the ratio of the resistance changes in sensing channels 1 and 2 (ΔR_1 or ΔR_2) in relation to the combined resistance change in both sensing channels ($\Delta R_1 + \Delta R_2$). In Fig. 3b, the experimentally determined pressure location index (shown in orange dot) for different sections of sensing channel 2 exhibited a linear decrease, closely matching the theoretically derived value (depicted in black dot). The theoretical value was calculated based on the expected resistance change ratios for the sensing channels. Supplementary Fig. 2b further illustrated that the pressure location index between sensing channel 1 (black dot) and sensing channel 2 (red

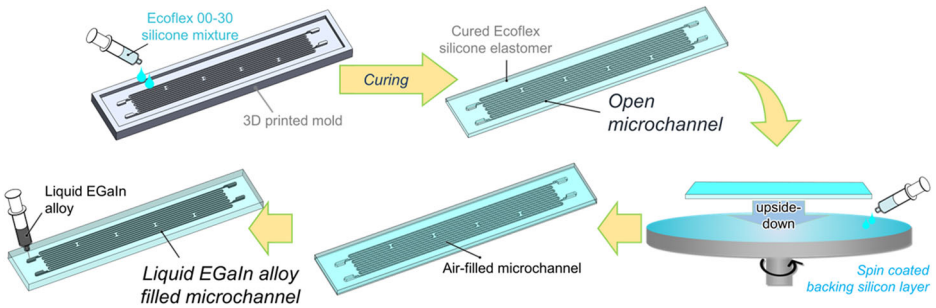

Fig. 1 | Schematic illustration of sensor fabrication. Uncured liquid EcoFlex 00-30 silicone was poured into a 3D-printed plastic mold with two sensing channels. The silicone was then cured, resulting in an open microchannels. This silicone mold was wet-bonded to a spin-coated silicone backing layer in an upside-down orientation to seal the open microchannel. Finally, the sensing material, EGaIn alloy, was injected into the previously air-filled microchannel using a syringe-assisted method.

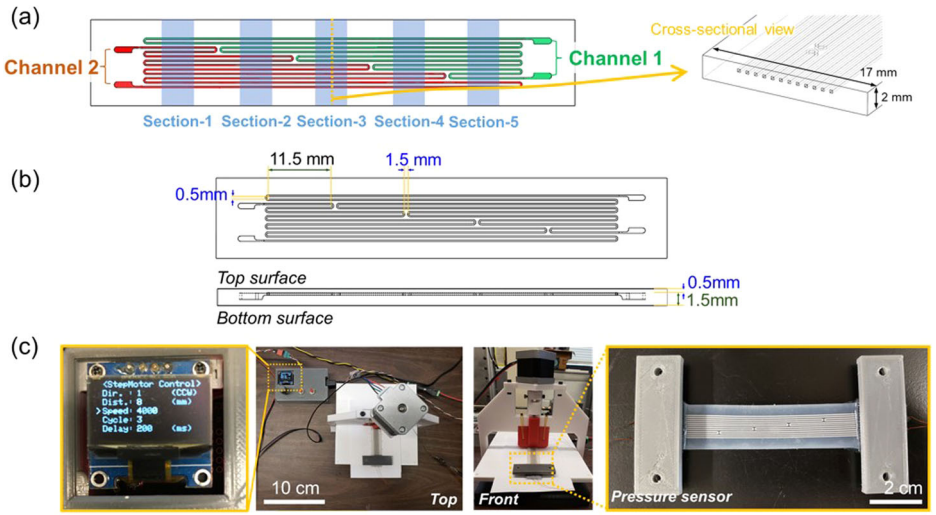

Fig. 2 | Design of the sensor and testing setup. **a** Schematic illustration of the pressure sensor design, **b** detailed information on sensor dimensions, and **c** photographic image of the pressure measurement setup with a motorized the pressure applying system. A custom-built tester applied pressure to the sensor, ranging from 0 to 0.1 MPa.

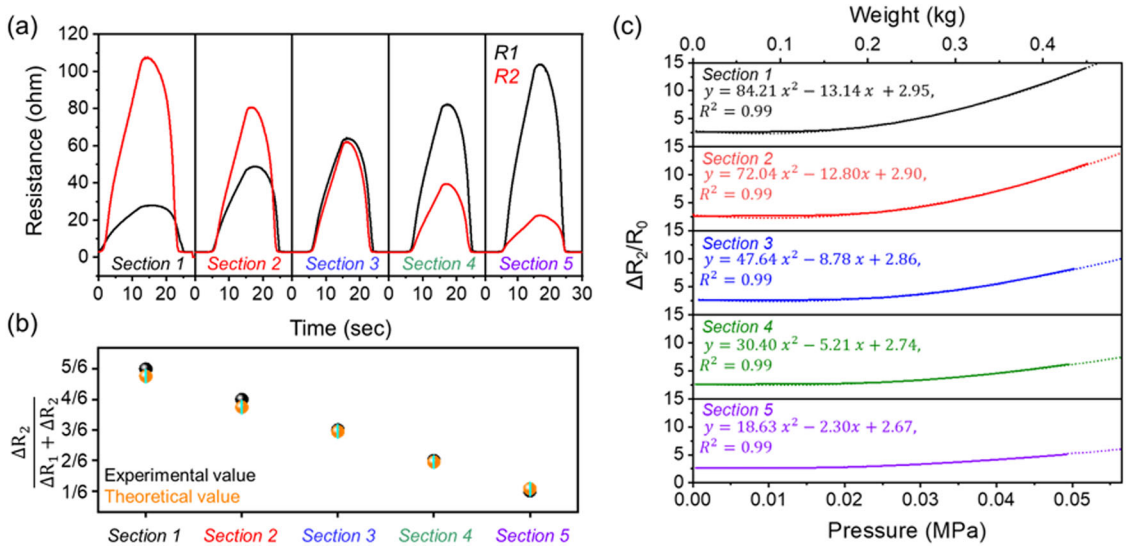

Fig. 3 | Pressure sensor test results. **a** Time-dependent sensor resistance variation during gradual pressure loading/unloading (up to 0.1 MPa) across five sections (Sections 1–5) over 30 s. **b** Pressure location index from sensing channel 2 is represented as the output resistance ratio $R_2/(R_1 + R_2)$. Resistances are taken from the peak resistance point of each section in (**a**), and the blue line indicates the error bar. The distinct index values per section align with theoretical predictions, confirming the sensor's ability to accurately identify applied pressure locations. **c** Resistance alterations in individual sections of sensing channel 2 as pressure gradually rises to 0.05 MPa (solid line) are accompanied by fitted parabolic equations (dotted line) expressed as $y = Ax^2 + Bx + C$, where y symbolizes relative resistance changes and x denotes pressure. The sensor's response fitting this parabolic equation emphasizes its extensive and reliable sensing range.

dot) displayed a contrasting trend, confirming the effectiveness of our sensor's design. Moreover, irrespective of the specific timing of the measurements (or the exact pressure at that moment), the pressure location indexes for sensing channel 1 (Supplementary Fig. 2c, upper graph) and sensing channel 2 (Supplementary Fig. 2c, lower graph) consistently aligned with the theoretical expectations. This highlights the reliability of the pressure location index as a dependable indicator of pressure location.

The performance of the sensor was further assessed, as depicted in Fig. 3c, where the pressure was gradually applied up to 0.05 MPa. On the y axis, R_0 represents the initial resistance value, and ΔR_2 denotes the resistance change observed in sensing channel 2 (sensing channel 1's response is showcased in Supplementary Fig. 3). The exerted pressure was derived from the weight loaded using the following equation:

$$P = F/A \tag{1}$$

Here, P stands for pressure, and F for force. The contact area, A, was measured to be 85 mm^2 (17 × 5 mm^2). The relative sensor response $\Delta R_2/R_0$ (or $\Delta R_1/R_0$ in Supplementary Fig. 3) was plotted against the applied pressure (or the applied weight) and fitted with a parabolic equation,

$$y = Ax^2 + Bx + C, \tag{2}$$

where y is the relative sensor response, and x is the applied pressure. In this context, a sensor's sensitivity can be derived from the slope of the output $(\Delta R/R_0)$ concerning the applied pressure ΔP, represented as Eq. (3)[15,17,35].

$$\text{Sensitivity } S = (\Delta R/R_0)/\Delta P \tag{3}$$

This sensitivity parameter, an essential aspect of sensor performance, was calculated to be 66.07 MPa^{-1} under an applied pressure of 0.05 MPa. The outstanding sensitivity of our sensor is attributed to the low Young's

modulus (~0.5 MPa) of the EcoFlex 00-30. The pressure given to the soft EcoFlex matrix induces the volume changes in the microchannels, resulting in a change in the resistance of the liquid metal. Even subtle pressure can directly influence the resistance variation of the liquid metal, thus achieving high sensitivity.

A cyclic test of the sensor was conducted, and the results are displayed in Fig. 4. Figure 4a shows the sensor's responses across sections 1–5 during 10 cycles of applied pressure ranging from 0 to 0.05 MPa. The progression of the applied pressure (i.e., weight) during the test is detailed in Supplementary Fig. 4. The results demonstrate that our sensor consistently performs across multiple measurement cycles in all sections 1 to 5 under the applied pressure, as shown in Fig. 4a. Figure 4b provides a zoomed-in view of the single pulses, specifically capturing the time frame between 80 and 160 s from Fig. 4a. From the data obtained from the single pulses shown in the results, we can calculate the signal-to-noise ratio (SNR). The SNR is crucial in determining the measurement resolution, which indicates the smallest change the sensor can detect. The measurement resolution is one of the critical parameters when evaluating the overall sensor performance. A lower SNR can limit the sensor's capacity to discern minor changes in pressure, underscoring the significance of this ratio in sensor performance. The SNR (dB) is determined using formula (4).

$$SNR(dB) = 20\log 10((\Delta R/R_{signal})/(\Delta R/R_{noise})) \quad (4)$$

Here, $\Delta R/R_{signal}$ represents the fractional resistance changes due to applied pressures, while $\Delta R/R_{noise}$ indicates the standard deviation of the resistance fluctuation under those pressures[35]. The sensor exhibited an average SNR value of 72.10 dB and a measurement resolution ($\Delta R/R_{noise}$/sensitivity) of 0.056 kPa, highlighting its superior performance. The durability of the sensor was evaluated by conducting 1000 cyclic tests in section 4 with a pressure of 0.08 MPa, and the results are depicted in Supplementary Fig. 5. Even under harsh conditions, the tested result was very reliable. A cyclic test with varying applied pressures from 0.01 to 0.06 MPa was conducted to check the sensor's reliability, and the response of sensing channels 1 and 2 in section 5 pressed with varying pressures is depicted in Fig. 4c and d. Remarkably, the resistance-changing curves for both R_1 and R_2 overlapped consistently across different applied pressures. This result indicates that the fitted parabolic equations depicted in Fig. 3c accurately represent a sensor performance with high reliability under wide pressure ranges. The sensor was further assessed by pressing with a larger dimension and a higher pressure of up to 0.6 MPa, and the following results are displayed in Supplementary Fig. 6. Supplementary Fig. 6a depicts resistance variation under pressure localized to section 4 (17×5 mm^2), while Supplementary Fig. 6b illustrates the resistance variation resulting from pressure applied across all the sections (17×90 mm^2) (pressed areas are highlighted with blue on the top of the figure). Irrespective of the pressing dimension or the pressure amount, the sensor resistance variations exhibited reliable results, and the related pressure location indexes highly matched the theoretical values, demonstrating the potential of the sensor as a gait monitoring sensor.

Sensors' extensive sensitivity and ability to accurately discriminate pressure applied location were evidenced by employing two applications: a piano (Supplementary Movie 1) and a joystick for car control (Supplementary Movie 2). For the experiment, the sensor was connected to Arduino UNO with an electronic circuit, as depicted in Supplementary Fig. 7, and the sensor sections were discriminated by adjusting the threshold of resistance changes. In both applications, the movies clearly illustrate that the suggested microchannel design successfully achieved sectional discrimination, while the remarkable sensor sensitivity allowed it to respond to light finger pressing.

A systematic evaluation of our fabricated pressure sensor's performance and efficiency was conducted, with results compared against previously reported research findings summarized in Table 1, with four categorized groups: EcoFlex-based[14–17], liquid metal-based[25–27,36–38], microchannel-based[23,39–41], and carbon-based pressure sensors[7,18,19,42]. Our sensor notably distinguishes itself with its extensive and reliable sensing range of 0 to 100 kPa and exceptional sensitivity of 66.07 MPa^{-1}. This remarkable achievement is exemplified in Fig. 3c, where the variations in sensor output resistance across different sections were well-modeled by a parabolic equation, which is an uncommon result compared to previously reported pressure sensors. Many sensors in previous studies exhibited a linear relationship between sensor output and applied pressure within a limited pressure range; thus, this limitation restricted their applicability to a narrow pressure range despite their high sensitivity[43,44]. In contrast, our sensor, owing to the hyperelastic properties of the EcoFlex substrate, can directly translate even subtle deformations of the substrate into variations in the shape of the EGaIn within the

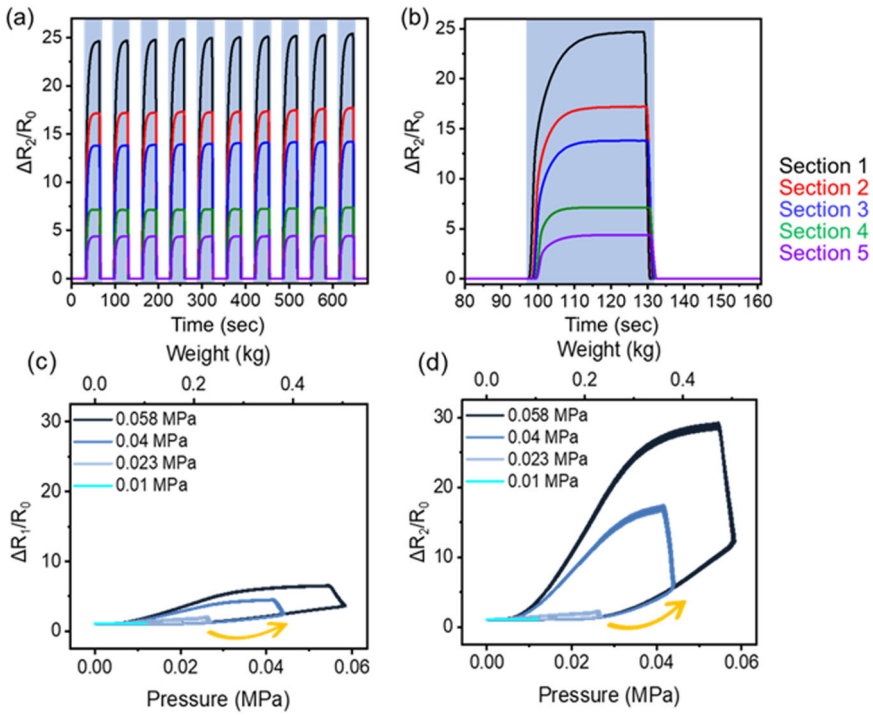

Fig. 4 | Cyclic test result of the sensor under an applied pressure up to 0.05 MPa. a Variation in sensor resistance of sensing channel 2 over time, with the specific periods of applied pressure highlighted in blue. **b** Zoomed-in view of the single pulses measured between 80 and 160 s from (**a**). **c**, **d** Hysteresis loop of R_1 and R_2, respectively, obtained from section 5 under varying applied pressures.

https://doi.org/10.1038/s43246-024-00570-9

Table 1 | Performance comparison of pressure sensors

	Ref.	Sensing type	Sensing material	Substrate	SNR (dB)	Measurement resolution (kPa)	Sensitivity (kPa^{-1})	Reliable sensing range (kPa)	Flexibility (stretch/compression)	# of fabrication steps
This work		Resistive	EGaIn	EcoFlex	72	0.056	66,070	0–100	250%	5
Ecoflex based Sensor	14	Capacitive	EcoFlex	ITO/PEN film	–	0.02	1.277	0–0.5	–	5
	15	Resistive	Graphene, MoS_2 nanoflake composite	EcoFlex	–	–	3.28	0.6–7.6	50%	8
	16	Capacitive	EcoFlex	EcoFlex/CNT nanocomposite thin film	–	0.0001– 0.0002	0.601	0–5	~80%	6
	17	Electric	PEDOT: PSS	EcoFlex	–	90	6.13	0–5	30%	10
Liquid metal-based Sensor	25	Capacitive	GaIn-BiInSn	PDMS	–	–	450	0–440	20%	6
	26	Capacitive	EGaIn	EcoFlex	–	0.012	39	0–1	94%	13
	36	Electric	EGaIn, N-doped graphene nanosheet	PDMS	–	0.0098 N (dimension unknown)	476	0–3.4	–	4
	37	Resistive	GaIn	Dragon skin	–	<0.016	0.158	0–50	20%	8
	38	Resistive	EGaIn	EcoFlex	–	15	56.6	0–40	100%	6
	45	Resistive	EGaIn	PVA/P(AAm-co-SMA)	–	–	19,940	0–38	2000%	5
Microchannel based Sensor	23	Resistive	EGaIn	EcoFlex/PET film	–	–	0.002	2–400	–	5
	40	Resistive	GaIn	PDMS	–	0.1	0.0835	0–60	–	7
	40	Resistive	EGaIn	Dragon skin	–	–	0.3	0–100	–	5
	41	Resistive	GaIn	SP-RF0900	–	0.031	0.923	31	–	4
Conventional carbon-based Sensor	7	Capacitive	Carbon nanofiber & MXene	–	–	0.005	65	0–0.010	95%/~50	10
	18	Electric	graphene & AuNPs	PDMS	–	0.044	5.37	<1	150%	8
	19	Resistive	MXene	PET	–	0.009	99.5	0–1	100%	7
	42	Resistive	Carbon Black & Multi-walled carbon nanotube	PDMS	–	–	3.57	~21	120%	8

microchannel. This property accounts for the pronounced changes in output resistance across a wide pressure range, thus contributing to the sensor's outstanding sensitivity. The fabrication method was notably simple and cost-effective as well. In contrast to other microchannel-based sensors that often rely on complex soft lithography for fabrication, our method successfully encapsulated the liquid metal within microchannels using a 3D-printed plastic mold, offering a simpler and more economical approach. The durability of the EcoFlex substrate allowed our device to stretch up to 250% without any EGaIn leakage, resulting in remarkable stretchability, sensitivity, and a wide reliable sensing range. Furthermore, the innovative microchannel architecture combined with pressure-sensitive materials elevated our sensor's capabilities, enabling it to distinguish the pressure-applied location precisely with a single device and widen the applicable area.

Application of the pressure sensor: wearable gait monitoring sensor

The pressure sensor we developed found practical application in gait monitoring, with a specific focus on analyzing the dynamic gait patterns of a

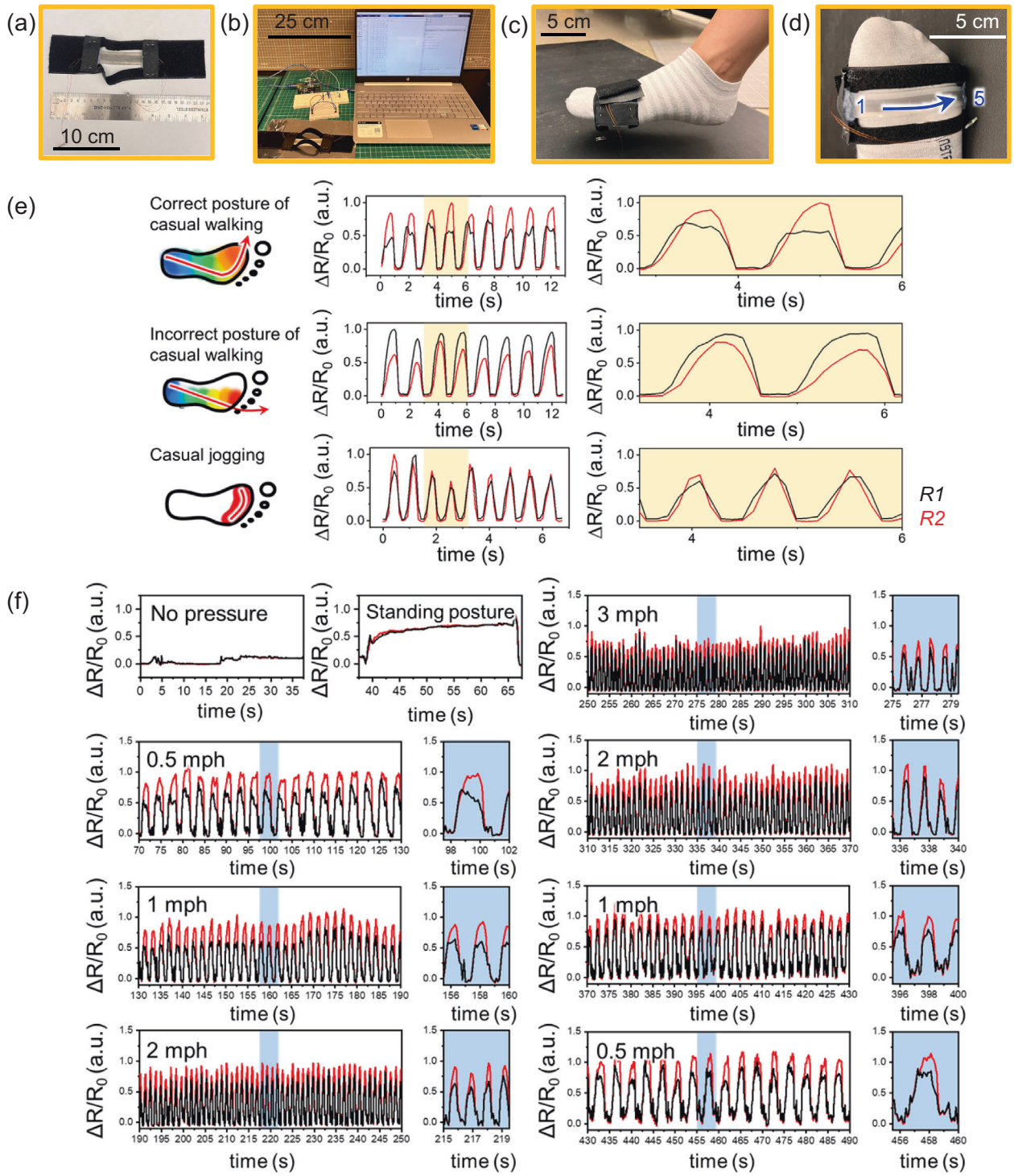

Fig. 5 | Application of pressure sensor as a gait monitoring system. a–d Digital images of the sensor and the test set up for gait monitoring, **e** resistance changes on walking and jogging cycles, and **f** resistance changes on different walking speeds on a treadmill with correct walking posture. In the conducted test, a series of experiments were performed to analyze the gait pattern during standing and walking at various speeds ranging from 0 to 3 mph.

single leg during motion. The sensor was affixed to the subject's right foot using a Velcro strap, as depicted in Fig. 5a. A detailed configuration illustrating the connection with an Arduino is provided in Fig. 5b. The sensor, attached via the Velcro strap, was strategically placed on the subject's right foot (underneath the ball joint of the forefoot, along distal ends of metatarsals) to span from beneath the thumb (section 1) to beneath the little toe (section 5), as illustrated in Fig. 5c and d. We proceeded to evaluate pressure distribution on the subject's right foot during both stationary and dynamic phases by recording the resistance changes of R_1 and R_2 throughout the gait cycle, with R_0 denoting the initial values of R_1 and R_2. The sensor placed on the forefoot facilitated an in-depth examination of the pressure distribution across the walking cycle. The subject was instructed to perform different gait postures, including correct walking (1 mph speed), incorrect walking (1 mph speed), and casual jogging (5 mph speed). The resistance changes corresponding to each posture are depicted in Fig. 5e. The results revealed distinct and specific patterns associated with different gait postures, and these patterns remained consistent throughout each testing duration, highlighting the sensor's capability to distinguish gait postures effectively.

To elucidate the detailed comparison between the postures, the graphs of resistance changes from 3.5 to 6 s were magnified as highlighted within yellow boxes. In the correct walking cycle, R_1 (black line) initially registered higher values than R_2 (red line), which can be interpreted as more pressure being applied to section 5, i.e., to the little toe. After a few seconds, the resistance values of R_1 and R_2 underwent a reversal, indicating the pressure was shifted from the little toe (section 5) to the thumb (section 1), as denoted by the red arrow in the foot diagram on the left side of the graph. On the other hand, in incorrect walking cycles, R_1 consistently exceeded R_2, suggesting sustained pressure on the little toe throughout the cycle. Meanwhile, in jogging cycles, R_1 and R_2 exhibited similar values, signifying uniform pressure distribution across the forefoot area.

To further explore the sensor's capabilities, the subject was tasked with walking on a treadmill at varying speeds (ranging from 0 to 3 mph) while maintaining the correct walking gait. Detailed images of the experimental setup and speed variations can be found in Supplementary Fig. 8. The resistance changes observed during this test are graphically depicted in Fig. 5f. When the sensor was not pressed (0–37.5 s) or evenly pressed (standing posture, 37.5–67.5 s), R_1 and R_2 showed comparable values. While walking at different speeds, the sensor consistently exhibited a specific pattern reflective of the correct walking posture. Regardless of the walking speed, R_1 (black line) initially showed prominence, which was then reversed by R_2, as clearly evident from the graphs highlighted in blue. Under the casual walking condition (1 mph), real-time wearable gait monitoring results were recorded on the laptop (see Supplementary Movie 3), and we found that the monitoring system distinguished the correct posture of casual walking very clearly. We enhanced the sensor's utility by developing a wireless data acquisition system using an Arduino MKR WiFi 1010 microcontroller with an electronic circuit, as depicted in Supplementary Fig. 9. The sensor was fixed to the subject's foot while the microcontroller was attached to the ankle (Supplementary Fig. 10a and b). The microcontroller transferred the collected data with various postures to a personal computer via an IP address and WiFi connection. As can be seen in Supplementary Movies 4 and 5, the sensor with the wireless system successfully collected real-time data while walking at different speeds. In Supplementary Fig. 10c, especially in the zoomed-in graph on the right side, the sensor showed a unique pattern of correct walking posture, coinciding with the wired system-based data in Fig. 5. This development improved the practicality of using the sensor during walking, thereby underscoring its potential for monitoring individuals with mobility impairments, including those with conditions such as Parkinson's disease or other walking challenges, in their rehabilitation efforts.

Methods

Pressure sensor fabrication

The mold for microchannels was prepared using rigid/durable Vero family photopolymer inks using a 3D printer (Objet500 Connex2 3D printer, Stratasys, Ltd). The dimension of the microchannels was designed as 250 μm × 125 μm, with a distance of 500 μm between the microchannels. To fabricate the substrate, EcoFlex 00-30 silicon prepolymer (Smooth-on, Inc.) was prepared by mixing the silicon parts with a ratio of 1:1. The prepolymer solution was spin-coated and cured to obtain the silicon-based microchannel substrate. EGaIn liquid alloy (Sigma-Aldrich, Inc.) was injected into the microchannels to complete the fabrication process. While filling in the EGaIn with a syringe, an additional syringe needle was inserted into the end of the microchannels to release any trapped air. Once the EGaIn alloy was evenly and thoroughly filled into the microchannels, the fabrication process was completed by connecting 32 AWG-enameled copper wires to the terminal ports of each sensing channel.

Measurements and characterizations

The performance of the pressure sensor was measured using a motorized pressure-applying system (shown in Fig. 2c). The motorized system controls the direction, pressed depth (distance), speed, cycles, and duration of the loading/unloading procedure. The sensor data was acquired using an NI USB-6251 data acquisition system along with an NI SCB068 module. The 5 V DC input voltage to the sensor is provided by the NI SCB-68 module, which measures the voltage change caused by the geometric deformation of the EGaIn microchannels induced by pressing the sensor.

Conclusion

In this paper, we have developed a highly sensitive pressure sensor tailored for gait monitoring applications. The sensor was fabricated using a cost-effective manufacturing process that capitalizes on the impressive ultra-stretchable properties of EcoFlex and EGaIn liquid alloy. Our sensor exhibited remarkable attributes, including non-linear changes in resistance when subjected to pressures up to 100 kPa, accompanied by an exceptional signal-to-noise ratio (SNR) value of 72 dB. The incorporation of two sensing channels and its innovative design allowed for the simultaneous measurement of both absolute pressure values and the precise localization of applied pressure. Consequently, the sensor displayed outstanding performance in accurately discerning various human gait postures. The outcomes of our sensor testing offer valuable insights, suggesting promising opportunities for its utilization in clinical applications and rehabilitation studies.

Data availability

The authors declare that the data supporting the findings of this study are available within the paper and its supplementary information files. Further data supporting the findings of this study are available from the authors upon reasonable request.

Received: 19 December 2023; Accepted: 11 July 2024;
Published online: 24 July 2024

References

1. Zhu, L., Wang, Y., Mei, D. & Jiang, C. Development of fully flexible tactile pressure sensor with bilayer interlaced bumps for robotic grasping applications. *Micromachines* **11**, 770 (2020).
2. Hema, K. Mems pressure sensor in automotive industry. *Int. J. Sci. Res.* **2**, 533–535 (2013).
3. Wang, Y., Chao, M., Wan, P. & Zhang, L. A wearable breathable pressure sensor from metal-organic framework derived nanocomposites for highly sensitive broad-range healthcare monitoring. *Nano Energy* **70**, 104560 (2020).
4. Kim, K. et al. All-soft multiaxial force sensor based on liquid metal for electronic skin. *Micro Nano Syst. Lett.* **9**, 2 (2021).
5. Guo, Y., Zhong, M., Fang, Z., Wan, P. & Yu, G. A wearable transient pressure sensor made with Mxene nanosheets for sensitive broad-range human–machine interfacing. *Nano Lett.* **19**, 1143 (2019).
6. Wang, Y. et al. Self-powered wearable pressure sensing system for continous healthcare monitoring enabled by flexible thin-film thermoelectric generator. *Nano Energy* **73**, 104773 (2020).

7. Qin, L. et al. Superelastic and ultralight electrospum carbon nanofiber/Mxene hybrid aerogels with anisotropic microchannels for pressure sensing and energy storage. *J. Colloid Interface Sci.* **589**, 264 (2021).
8. Tian, H. et al. A graphene-based resistive pressure sensor with record-high sensitivity in a wide pressure range. *Sci. Rep.* **5**, 8063 (2015).
9. Sorkin, V. & Zhang, Y. W. Graphene-based pressure nano-sensors. *J. Mol. Model.* **17**, 2825 (2011).
10. Smith, A. D. et al. Electromechanical piezoresistive sensing in suspended graphene membranes. *Nano Lett.* **13**, 3237 (2013).
11. Chen, S. et al. Fabrication and piezoresistive/piezoelectric sensing characteristics of carbon nanotube/PVA/nano-ZnO flexible composite. *Sci. Rep.* **1**, 8895 (2020).
12. Qin, R. et al. A new strategy for the fabrication of a flexible and highly sensitive capacitive pressure sensor. *Microsyst. Nanoeng.* **7**, 100 (2021).
13. Sanati, M., Sandwell, A., Mostaghimi, H. & Park, S. S. Development of nanocomposite-based strain sensor with piezoelectric and piezoresistive properties. *Sensors* **18**, 3789 (2018).
14. Kim, S. W. et al. A highly sensitive and flexible capacitive pressure sensor based on alignment airgap dielectric. *Sensors* **22**, 7390 (2022).
15. Kim, S. J., Mondal, S., Min, B. K. & Choi, C. G. Highly sensitive and flexible strain-pressure sensors with cracked paddy-shaped MoS_2/graphene foam/Ecoflex hybric nanostructures. *ACS Appl. Mater. Interfaces* **10**, 36377 (2018).
16. Kwon, D. et al. Highly sensitive, flexible, and wearable pressure sensor based on a giant piezocapacitive effect of three-dimensional microporous elastomeric dielectric layer. *ACS Appl. Mater. Interfaces* **8**, 16922 (2016).
17. Han, S. et al. High-performance pressure sensors based on 3D microstructure fabricated by a facile transfer technology. *Adv. Mater. Technol.* **4**, 1800640 (2019).
18. Wang, J. et al. Fabrication of a sensitive strain and pressure sensor from gold nanoparticle-assembled 3D-interconnected graphene microchannel-embedded PDMS. *ACS Appl. Mater. Interfaces* **12**, 51854 (2020).
19. Gao, Y. et al. Microchannel-confined Mxene based flexible piezoresistive multi-functional micro-force sensor. *Adv. Funct. Mater.* **30**, 1909603 (2020).
20. Yang, X., Wang, Y. & Qing, X. A flexible capacitive pressure sensor based on ionic liquid. *Sensors* **18**, 2395 (2018).
21. Kim, M.-G., Brown, D. K. & Brand, O. Nanofabrication for all-soft and high-density electronic devices based on liquid metal. *Nat. Commun.* **11**, 1002 (2020).
22. Varga, M., Ladd, C., Ma, S., Molbery, J. & Troster, G. On-skin liquid metal inertial sensor. *Lab Chip* **19**, 3272 (2017).
23. Yeo, J. C. et al. Triple-state liquid-based microfluidic tactile sensor with high flexibility, durability, and sensitivity. *ACS Sens.* **1**, 543 (2016).
24. Tetsu, Y. et al. Ultrathin epidermal strain sensor based on an elastomer nanosheet with an inkjet-printed conductive polymer. *Appl. Phys. Express* **10**, 087201 (2017).
25. Zhang, L., Gao, M., Wang, R., Deng, Z. & Gui, L. Stretchable pressure sensor with leakage-free liquid metal electrodes. *Sensors* **19**, 1316 (2019).
26. Zhang, Y. et al. Highly stretchable and sensitive pressure sensor array based on icicle-shaped liquid metal film electrodes. *ACS Appl. Mater. Interfaces* **12**, 27961 (2020).
27. Chen, J. et al. A liquid metal based super-stretchable strain sensor. In *2018 IEEE 13th Annual International Conference on Nano/Micro Engineered and Molecular Systems (NEMS)* 377 (IEEE, 2018).
28. Guo, Q. et al. Microchannel structural design for a room-temperature liquid metal based super-stretchable sensor. *Sci. Rep.* **1**, 5908 (2019).
29. Chen, J. et al. Superelastic, sensitive, and low hysteresis flexible strain sensor based on wave-patterned liquid metal for human activity monitoring. *ACS Appl. Mater. Interfaces* **19**, 22200 (2020).
30. Cooper, C. B. et al. Stretchable capacitive sensors of torsion, strain, and touch using double helix liquid metal fibers. *Adv. Funct. Mater.* **20**, 1605630 (2017).
31. Kim, S. et al. Stretchable and soft electroadhesion and capacitive sensors enabled by spider web-inspired interdigitated liquid metal subsurface microwires. *Chem. Eng. J.* **456**, 141018 (2023).
32. Xu, C., Mei, D., Zhy, L. & Wang, Y. Flexible capacitive pressure sensor array using acoustic-assisted fabrication of microstructures as surface and dielectric layers. *Sens. Actuator A-Phys.* **248**, 114006 (2022).
33. Kim, S. et al. EgaIn-Silicone-based highly stretchable and flexible strain sensor for real-time two joint robotic motion monitoring. *Sens. Actuators A-Phys.* **342**, 113659 (2022).
34. Shin, S., Yoon, H. U. & Yoo, B. Hand gesture recognition using EGaIn-silicone soft sensors. *Sensors* **9**, 3204 (2021).
35. Kim, S. et al. Piezoresistive graphene/P(VDF-TrFE) heterostructure based highly sensitive and flexible pressure sensor. *ACS Appl. Mater. Interfaces* **11**, 16006 (2019).
36. Li, Y. et al. Ultrasensitive pressure sensor sponge using liquid metal modulated nitrogen-goped graphene nanosheets. *Nano Lett.* **22**, 2817 (2022).
37. Kim, K. et al. Highly-sensitive and wearable liquid metal-based pressure sensor for health monitoring applications: Integration of a 3D-printed microbump array with the microchannel. *Adv. Healthc. Mater.* **8**, 190978 (2019).
38. Li, X. et al. Self-healing liquid metal hydrogel for human–computer interaction and infrared camouflage. *Mater. Horiz.* **10**, 2945 (2023).
39. Gao, Y. et al. Wearable microfluidic diaphragm pressure sensor for health and tactile touch monitoring. *Adv. Mater.* **29**, 1701985 (2017).
40. Huang, H. et al. Research progresses in microstructure designs of flexible pressure sensors. *Polymers* **14**, 3670 (2022).
41. Wang, Y., Jin, J., Lu, Y. & Mei, D. 3D printing of liquid metal based tactile sensor for simultaneously sensing of temperature and forces. *Int. J. Smart Nano Mater.* **12**, 269 (2021).
42. Yuan, J. et al. Carbon black/multi-walled carbon nanotube-based, highly sensitive, flexible pressure sensor. *ACS Omega* **7**, 44428 (2022).
43. Tee, B. C. K., Wang, C., Allen, R. & Bao, Z. An electrically and mechanically self-healing composite with pressure- and flexion-sensitive properties for electronic skin applications. *Nat. Nanotechnol.* **7**, 825 (2012).
44. Wang, Y., Gong, S., Wang, S. J., Simon, G. P. & Cheng, W. Volume-invariant ionic liquid microbands as highly durable wearable biomedical sensors. *Mater. Horiz.* **3**, 163 (2016).
45. Park, Y.-L. Design and fabrication of soft artificial skin using embedded microchannels and liquid conductors. *IEEE Sens. J.* **12**, 3711 (2012).

Author contributions

The idea of the study was conceived by J.-B. Ahn, B. Yoo, D.J. Pines, and S. Kim. J.-B. Ahn and B. Yoo conducted sensor fabrication and all measurements and wrote a major part of the paper under the supervision of S. Kim. C.-Y. Kuo, M. Wang, and N.S.G. Bejjanki designed the circuit for wireless signal transmission and wrote the code for signal analysis, and the wireless system was developed and analyzed with J.-B. Ahn and S. Kim. All authors contributed to the manuscript and J.-B. Ahn, B. Yoo, and S. Kim revised the manuscript.

Competing interests

The authors declare no competing interests.

Additional information

Supplementary information The online version contains supplementary material available at https://doi.org/10.1038/s43246-024-00570-9.

Correspondence and requests for materials should be addressed to Soaram Kim.

Peer review information *Communications Materials* thanks Michael Dickey and the other, anonymous, reviewer(s) for their contribution to the peer review of this work. Primary Handling Editor: John Plummer.